Neutron and light-charged-particle productions in proton-induced reactions on ^{208}Pb at 62.9 MeV

A. Guertin[1], N. Marie[2,a], S. Auduc[1], V. Blideanu[2], Th. Delbar[4], P. Eudes[1], Y. Foucher[1], F. Haddad[1], T. Kirchner[1], Ch. Le Brun[2,b], C. Lebrun[1], F.R. Lecolley[2], J.F. Lecolley[2], X. Ledoux[3], F. Lefèbvres[2], T. Lefort[2], M. Louvel[2], A. Ninane[4], Y. Patin[3], Ph. Pras[3], G. Rivière[1], and C. Varignon[2]

[1] Laboratoire Subatech, F-44307 Nantes cedex 03, France
[2] Laboratoire de Physique Corpusculaire, F-14050 Caen cedex, France
[3] Département de Physique Théorique et Appliquée, Service de Physique Nucléaire, B.P. 12, F-91680 Bruyères-le-Châtel, France
[4] Institut de Physique Nucléaire, B-1348 Louvain-la-Neuve, Belgium

Abstract. Neutrons and light charged particles produced in 62.9 MeV proton-induced reactions on ^{208}Pb were measured during a single experiment performed at the CYCLONE facility in Louvain-la-Neuve (Belgium). Two independent experimental set-ups were used to extract double differential cross-sections for neutrons, protons, deuterons, tritons, ^{3}He and alpha-particles. Charged particles were detected using a set of Si-Si-CsI telescopes from 25° to 155°, by step of 10 degrees. Neutrons were measured using shielded DeMoN counters, liquid NE213 scintillators, at 24°, 35°, 55°, 80° and 120°. These data allowed the determination of angle differential, energy differential and total production cross-sections. A comparison with theoretical calculations (MCNPX, FLUKA and TALYS) has been performed. It shows that the neutron and proton production rates are well predicted by MCNPX, using the INCL4 option. All the other codes underestimate the neutron production whereas they overestimate the proton one. For composite particles, which represent 17% of the charged particle total reaction cross-section, neither the shape nor the amplitude of the cross-sections are correctly predicted by the models.

PACS. 27.80.+w $190 \leq A \leq 219$ – 25.40.-h Nucleon-induced reactions – 25.40.Sc Spallation reactions

1 Introduction

For several years, there has been a revival interest on the use of neutrons in physics. Indeed, neutrons are useful tools in many fields of sciences such as material science studies [1], biology [2], isotope production for medical applications [3], radiation damage on electronic devices [4], nuclear energy and waste [5,6]. In all these cases, intense neutron sources are needed and the development of spallation sources offers a promising way [7,8].

A spallation source consists in an intense high-energy proton beam hitting a high atomic number target. Protons interacting with the target produce mostly neutrons ($\approx$ 1 per 25 MeV of the incident proton energy) via (p, xn) and secondary (n, xn) reactions, but also a large number of charged particles (protons, deuterons, tritons, ^{3}He, α-particles, ...) over a wide energy range, up to the incident nucleon energy. The neutron source thus created

^{a} e-mail: marie@lpccaen.in2p3.fr
^{b} *Present address*: Laboratoire de Physique Subatomique et de Cosmologie, F-38026 Grenoble cedex, France.

can be coupled, for example, with a sub-critical reactor to act as an additional external source. Such a system, called accelerator-driven system (ADS) [9], may allow the transmutation of the most radiotoxic nuclear waste.

In order to predict neutron production, shielding requirements, activation and material damage of these kinds of system, it is necessary to make macroscopic simulations that rely on basic nuclear reaction data. These data can be obtained directly from experimental results when they exist or using theoretical models. Below 20 MeV, extensive sets of data exist and are available in data libraries [10,11]. Above 200 MeV, the intranuclear cascade model is reliable and can be used to estimate accurately the needed cross-sections [12]. In the energy region between 20 MeV and 200 MeV, where very few experimental results are available, the situation is much more complicated since several reaction mechanisms contribute to the particle production. In addition, new reaction channels appear, implying the creation of composite particles. All these effects require a quite complex theoretical treatment especially to describe the production of light charged particles (lcp).

To address this problem, new nuclear data libraries for incident nucleons up to 200 MeV are beeing proposed. Since it is not possible within a reasonable time to provide them with experimental data, it has been decided to produce evaluated data, which are elaborated using state of the art theoretical models, in combination with a set of new experimental cross-sections [13]. This method ensures a good link between low and high-energy processes.

A large concerted program of nuclear data measurements, named HINDAS (High and Intermediate Nuclear Data for Accelerator-Driven Systems) [14], has therefore been set by European laboratories. It is intended to gather numerous observables from particle cross-section measurements to residue cross-sections for nucleon-induced reactions on specific nuclei. Only three candidates, Fe, Pb and U, have been chosen. They provide a sufficiently broad coverage of the periodic table and are also representative, respectively, of the structure, the target, and core materials (actinides) of an ADS. Neutron data are of great importance for neutron source applications. However, since neutron beams have lower intensities compared to protons, it is easier to perform proton-induced reactions and to measure (p, xn) channels rather than (n, xn) channels.

By a combination of both neutron and proton reactions, one should put enough constraints on ingredients of theoretical models. This large set of data will be used as benchmark points by code developpers helping them in their quest to enhance the predictive power of their theoretical models. Double differential production cross-sections in nuclear reactions induced by protons on a lead target are among HINDAS requested observables. These data are of great importance since, in general, theoretical models of nuclear reactions try only to reproduce energy differential cross-sections. The information contained in the double differential cross-sections (ddcs) is much more stringent, due to the strong angular dependance of pre-equilibrium reactions which are playing an important role in the 20–200 MeV energy region. Besides pre-equilibrium reactions, the direct interaction contribution at the high-energy part of spectra and the statistical evaporation component at the low-energy side have also to be taken into account in theoretical models.

The aim of this paper is to present our proton-induced (62.9 MeV) experiment on an enriched lead target ^{208}Pb performed on the S-line of the CYCLONE facility in Louvain-la-Neuve. In this experiment, two independant experimental set-ups were used to measure at the same time neutrons along with lcp ($Z = 1$ and $Z = 2$ isotopes) at various angular positions. The measured ddcs allowed also to determine integrated cross-sections with a good accuracy. This experiment followed a previous one with a neutron beam performed at the same incident energy [15].

Experimental set-ups and analysis schemes are presented in sect. 2, for both charged-particles and neutrons. In sect. 3, neutron and light-charged-particle double differential production cross-sections, angular differential and energy differential cross-sections are presented. In sect. 4, comparisons with theoretical calculations are performed. Finally, the conclusions of this work are given in sect. 5.
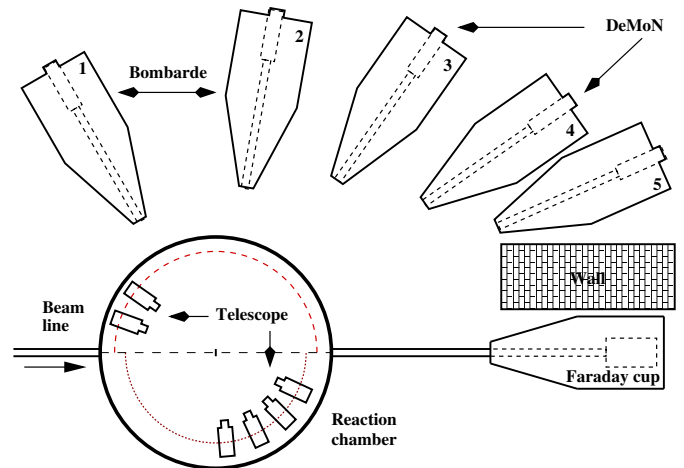

Fig. 1. Schematic view of the two independent set-ups.

2 Experimental set-ups and data analysis

The 62.9 MeV proton beam was delivered by the 18 MHz cyclotron of Louvain-la-Neuve. In order to be able to detect the low-energy neutrons, a kicker was used to reject eight beam bursts over nine, resulting in an interval of 500 ns between projectile bursts inside the experimental area. The experiment intended to measure, at the same time, neutrons and light charged particles. Two independent set-ups were used to achieve this goal. A set of seven telescopes was used for the charged-particle detection. They surrounded the target placed at the center of the reaction chamber. Neutrons were detected using five shielded devices placed inside "Bombarde" barrels (see sect. 2.2 for details). Their energies were determined with the time-of-flight (tof) technique. A schematic view of the whole experimental set-up is presented in fig. 1.

The beam was dumped four meters dowstream the chamber inside a Faraday cup whose integrated current was used for the beam monitoring. To shield detectors from the very high neutron flux resulting from the proton beam dump, the Faraday cup was also embedded inside a Bombarde barrel and a large wall, made of concrete and parafine, was built close to the dead end of the beam.

Several different targets were used during the experiment. They were mounted on a holder together with a quartz, viewed by a TV camera, for beam alignment and focussing. Target positions and orientations were adjusted with a remote control, in order not to break the vacuum. The calibration of detectors was performed using $(C_3H_6)_n$ (4.47 mg/cm^2) and ^{12}C (8.96 mg/cm^2) targets. An enriched ^{208}Pb target, of 10.7 mg/cm^2 thick, was used for the ddcs measurements. During the experiment, attention was paid to alternatively collect data with the ^{208}Pb target and with a blank target. This procedure enables to subtract the background noise from the data and then to estimate the number of particles produced in ^{208}Pb (p, xn) and ^{208}Pb $(p, x$lcp$)$ reactions. The acquisition dead time was also kept under 20% and a correction for this effect has been applied to the data.
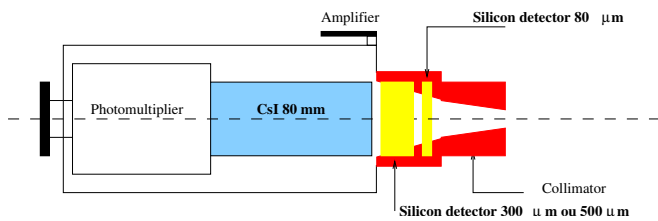
Fig. 2. Schematic view of one triple telescope (Si-Si-CsI).

2.1 Light-charged-particle detection

Light charged particles were detected using a set of seven triple telescopes (Si-Si-CsI) placed the vacuum chamber. A schematic view of a telescope is presented in fig. 2.

Each telescope consisted of two silicon detectors (80 μm thick (Si1) and 300 or 500 μm thick (Si2) respectively), backed by a one inch diameter and 80 mm thick CsI(Tl) crystal. It allowed us to identify and to measure light charged particles over their entire energy range. A copper collimator was placed in front of each telescope to precisely define the detection solid angle. The thickness of the first silicon detector determined the low-energy thresholds of our set-up, which were, respectively, 2.5 MeV for protons, 3 MeV for deuterons, 3.5 MeV for tritons, 9 MeV for ^{3}He and 10 MeV for alpha-particles.

A group of four telescopes was mobile and allowed us to record data from 25° up to 95° by step of 10°, and at 115°. During all the experiment, three telescopes were set at fixed positions. Two were set at 135° and 155° in order to accumulate sufficient statistics at these backward angles. The last one was set at 30° to be used as a second beam monitor along with the Faraday cup.

The identification of charged particles was obtained using the well known ΔE-E method.

The two first stages of telescopes (Si1-Si2) were used for the slowest particles (fig. 3), while the two last stages (Si2-CsI) take over for the most energetic ones (fig. 4).

In addition, most of the background coming from gamma rays was suppressed using a pulse shape analysis of the CsI energy signal. By combining the information contained in these different plots, an unambiguous particle identification was obtained for the full energy range.

To get silicon calibration curves, we used a three–alpha-particle source (Pu, Am and Cu) and the H(p, p) reaction at large angles for which the energy deposition in the second silicon detector is significant. The energy calibration of the CsI was achieved for each type of particle based on the kinematics of reactions on $(C_3H_6)_n$ target. The H(p, p) reaction allowed, by changing the detector angular position, to detect outgoing protons with energy from 51.7 MeV at 25° to 11.2 MeV at 65°. Calibration peaks for composite particles were obtained from nuclear reactions on ^{12}C.

Low-energy data points were obtained using the information delivered by the silicon detector and the energy loss data tables. This cross calibration allows us to obtain data points all over the energy range of interest. The
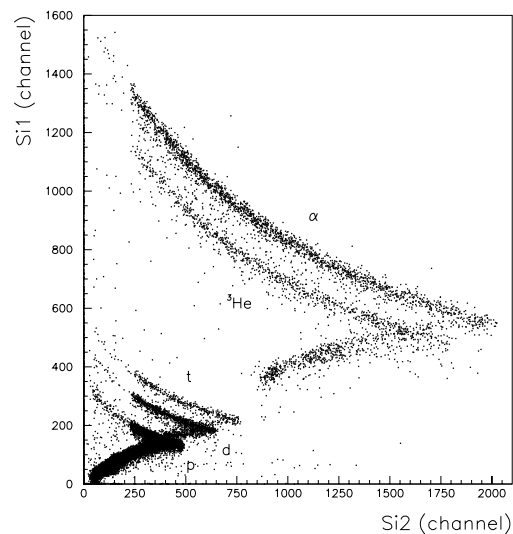
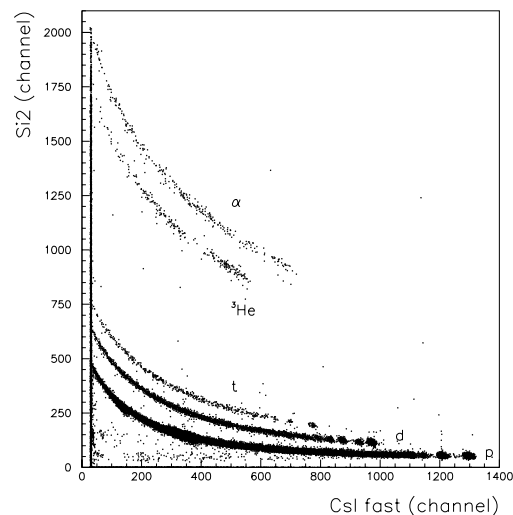

Fig. 3. Si1-Si2 spectra for a carbon target at 45°.

Fig. 4. Si2-CsI spectra for a carbon target at 45°.

achieved energy resolution is lower than the chosen histogram binning (1 MeV).

Nuclear reactions may occurred in the CsI which lead to a wrong determination of the particle energy. A quantitative study of this effect has been done for CsI counters at TSL [16] using protons with kinetic energies ranging from 40 MeV up to 80 MeV. Below 60 MeV, the CsI efficiency is almost constant and is compatible with 100%, considering the error associated to the experimental method. Therefore, in our analysis, we considered the CsI as fully efficient.

2.2 Neutron detection

Neutrons were detected using five DeMoN counters [17]. Each counter was composed of a 16 cm diameter and 20 cm deep cylinder, filled with NE213 liquid scintillator
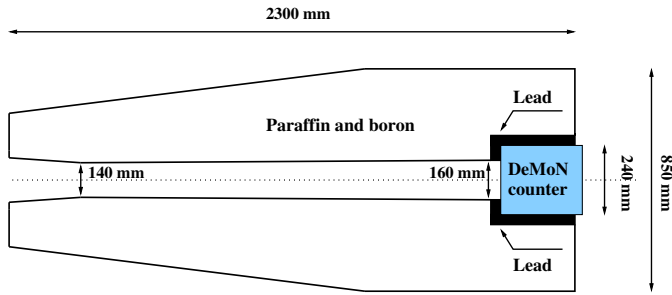
Fig. 5. Schematic view of a DeMoN counter installed inside its Bombarde barrel.
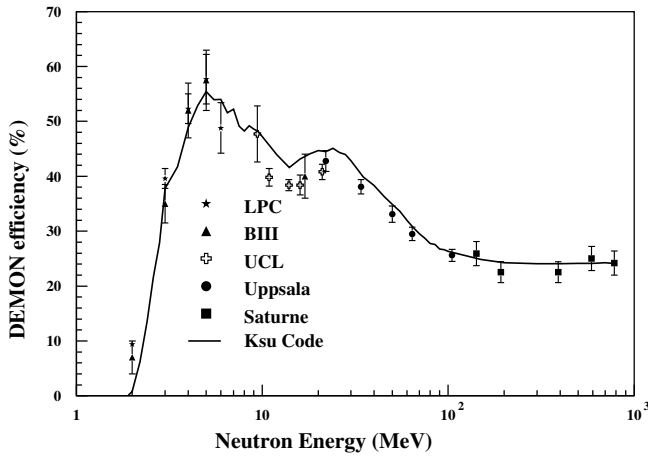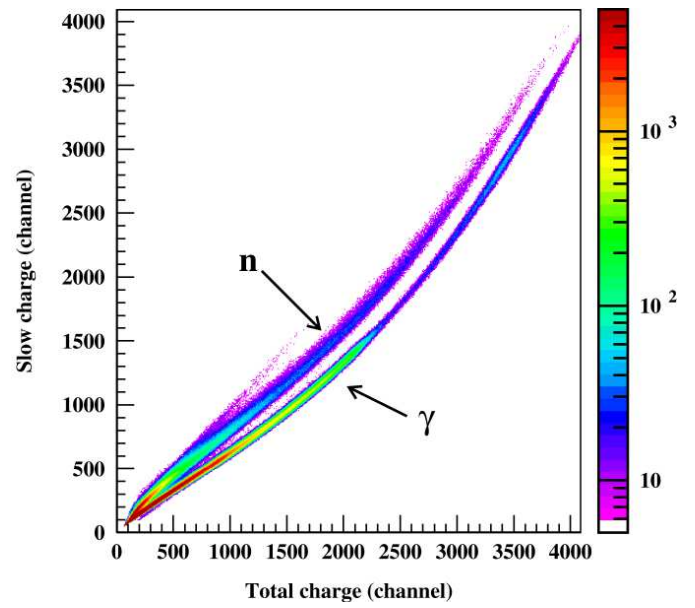

Fig. 6. Compilation of measured DeMoN detector efficiencies (symbols) compared to predictions of the KSU code (solid line).
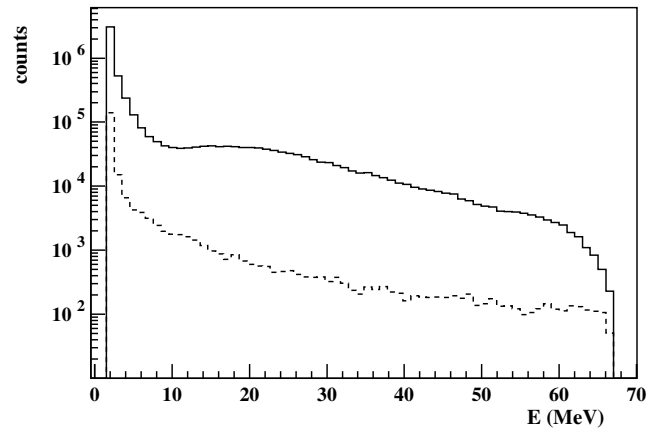

Fig. 7. Example of a DeMoN counter identification matrix.

Fig. 8. Typical example of two energy spectra obtained with a target and with a blank target at $35°$.

coupled with a XP4512 photomultiplier. Detectors were placed at $24°$, $35°$, $55°$, $80°$ and $120°$, and their time-of-flight path lengths were respectively 5.347 m, 3.887 m, 3.039 m, 2.507 m and 2.960 m. Each DeMoN counter was surrounded by a 4 cm thick lead cylinder and installed inside a Bombarde barrel filled with paraffin and boron. Those materials are efficient shields against background neutrons. A description of those massive tanks can be found in ref. [18]. A schematic view of a DeMoN counter housed in its Bombarde barrel is presented in fig. 5. The use of Bombarde barrels and of a shielding wall results in a signal-to-noise ratio of 33 for the most exposed detector to the parasite neutron flux.

A compilation of measured DeMoN detector efficiencies [19] is presented, as a function of the neutron energy, in fig. 6 together with predictions of the KSU code (solid line) [20,21]. Since the calculations produce measured efficiencies well, we have taken in our analysis the predicted values.

A very good discrimination between neutrons and gamma rays was achieved by pulse shape analysis of the liquid-scintillator response. An example of an identification matrix is presented fig. 7. The separation between gamma rays and neutrons is done by drawing a line in between both branches observed in the matrix. In order

to achieve a complete discrimination and eliminate the region where gamma rays and neutrons are mixed up, we have imposed a light integrated total charge threshold of 500 keV equivalent electron. This value is equivalent to a neutron energy threshold of 2 MeV [21]. Above that threshold, the separation is independent of the energy of the particles. The discrimination method employed is very efficient and the misidentification is very small as it can be seen by the quality of the matrix. Commonly, this method enables to reject 95 to 99% of the gammas, above the identification threshold.

Neutron energies were determined with the time-of-flight method. The time of flights were obtained from the signals given by the DeMoN counter and the beam kicker. They were measured with an electronic module having a precision of 500 ps. The neutron energies were derived
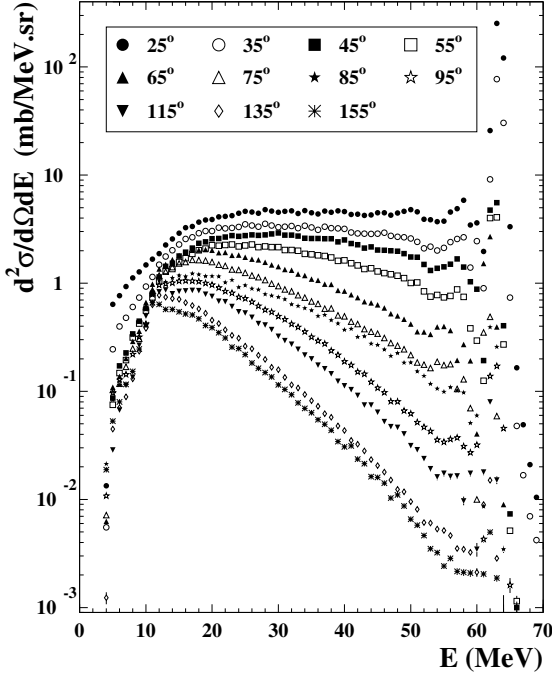
Fig. 9. ^{208}Pb(p, xp) double differential production cross-section at 62.9 MeV.

Fig. 10. ^{208}Pb(p, xd) double differential production cross-section at 62.9 MeV.
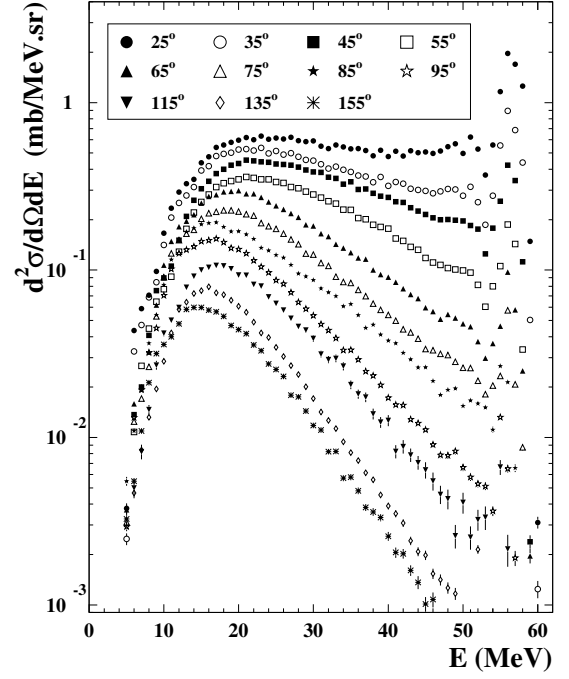
Fig. 11. ^{208}Pb(p, xt) double differential production cross-section at 62.9 MeV.

taking into account the mean depth at which the particle interacts inside the detector [22]. For all detectors and over the entire energy range, that depth varies between 8.6 cm and 10.3 cm. Concerning the measurement of the ambient neutron background, fig. 8 shows a typical example of two energy spectra obtained with a target and with a blank target. They were measured at 35°. We observe that the ambient neutron background has a decreasing exponential-like shape. It represents less than 10% of the total signal, for all angles, over the full energy range, except above 50 MeV where it can reach 25% and at 120° where the percentage increases rapidly with energy, because of the low counting rates measured at high energy and for backward angles.
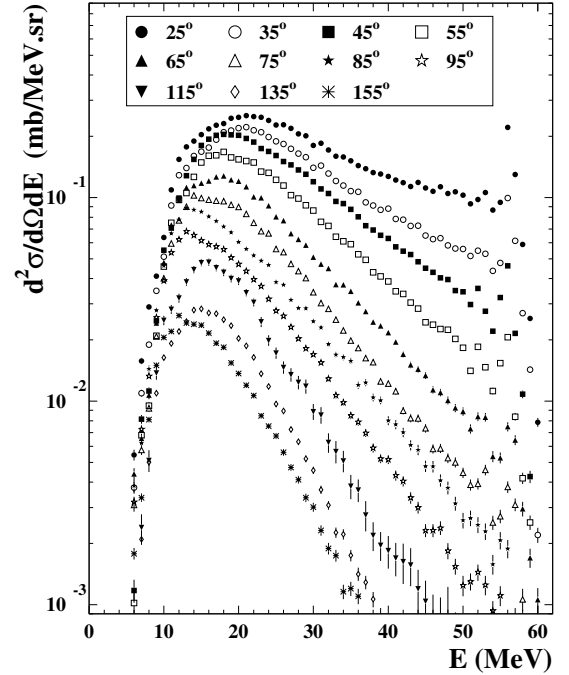
3 Experimental results

3.1 Light-charged-particle double differential cross-sections

Double differential production cross-sections for protons (p), deuterons (d), tritons (t), ^{3}He and alpha-particles (α) are reported for eleven angular positions, ranging from 25° to 155°, on figs. 9, 10, 11, 12 and 13, respectively.

Energy bins of 1 MeV have been used for all type of particles but ^{3}He (2 MeV). Only the statistical error is presented in our figures. The systematic error is estimated to about 6%. It was derived from the beam monitoring (5%), solid angle corrections (1%) and the number of target nuclei (3%).

Light-charged-particle spectra show generally the same characteristics and can be divided into three regions. In

the high-energy part of the spectra one can observe direct processes. In the case of protons, see fig. 9, it correponds mainly to elastic scattering on lead (see above 55 MeV). For deuterons, a peak coming from n(p,d) sub-processes is present at forward angles. Peaks are also found
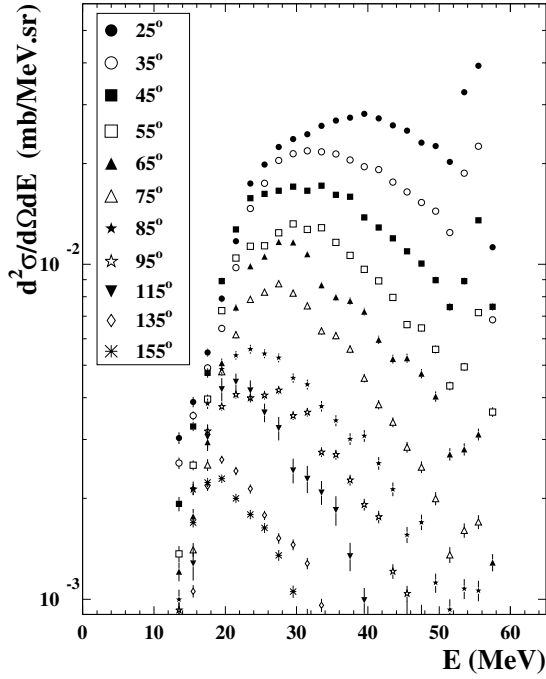
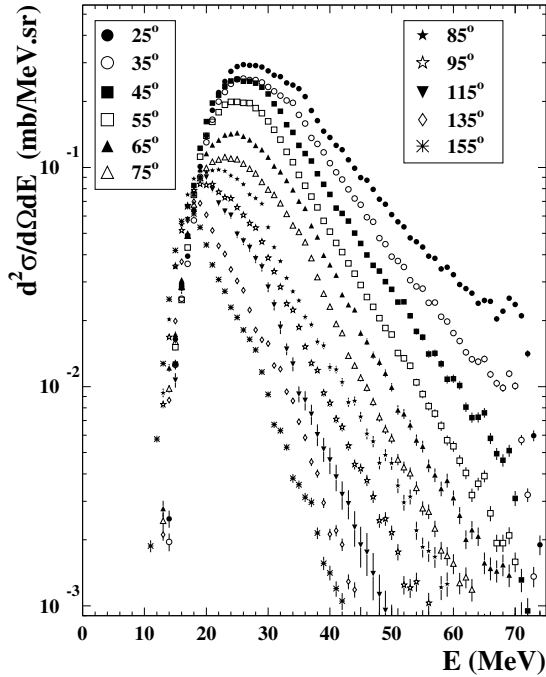**Fig. 12.** ^{208}Pb(p, x^3He) double differential production cross-section at 62.9 MeV.

Fig. 13. ^{208}Pb(p, $x\alpha$) double differential production cross-section at 62.9 MeV.

for tritons and ^{3}He. For α-particles, a careful study of the data suggests also the presence of a weak structure. The peak intensity is sensitive to the detection angle, suggesting that direct processes are highly non isotropic and correspond to a forward focus componant.

At backward angles ($\theta \geq 115°$), production spectra exhibit the characteristic shape of the evaporation pro-

cess of particles from a compound nucleus [23]. This phenomenon is isotropic and populates preferentialy the low-energy region. An evaporation peak cannot be observed. This lack is not due to a detection threshold but rather to the Coulomb barrier which is too high with the lead target and which inhibits the evaporation of low-energy lcp. Such a component could be observed with lighter targets in [24]. The influence of the barrier explains the observed progressive shift of the most probable energy value with the particle charge number and mass. The evaporation contribution can be quantified by looking at the most backward angles, since the spectra remain almost the same, in shape and magnitude, at 135° and 155°.

Below 115°, spectra show a strong angular dependence characteristic of pre-equilibrium processes. For protons, at the most forward angles, the spectra are almost flat, then, as the detection angle increases, they decrease rapidly in magnitude and they become steeper. The most energetic particles are produced mainly at forward angles but, even at the largest ones, protons can be observed with the maximum energy allowed. This behavior is characteristic of a production totally dominated by pre-equilibrium effects. This intermediate energy domain is also called "multiple-scattering region". Before escaping the target, the incident proton can undergo many collisions with individual nucleons inside the nucleus. An incident proton, which escapes the target after a first collision, will populate the highest energies. After a second collision, the projectile has lost more energy and then it will appear at slightly lower energies. This part of the spectra can then be understood as a combination of cross-sections of first, second, third, and so on, collisions. The target nucleons, which were knocked on along the path of the projectile, can also escape the nucleus and they will also contribute to the spectra. The deuteron spectra present the same evolutions as for protons. For tritons and ^{3}He, we observe almost the same features, except that the spectra exhibit a slight decrease with the energy even at the most forward angles. For alpha, the spectra have totally different shapes with slopes well pronounced at all angles.

We checked that the charged particle double differential cross-sections that we extracted are comparable to those previously measured on ^{209}Bi, at 62 MeV [24].

3.2 Neutron double differential cross-sections

Experimental neutron production double differential cross-sections are presented in fig. 14 for five different angles: 24°, 35°, 55°, 80° and 120°. When we constructed the energy spectra, we chose a bin size of 1 MeV, and we distributed uniformly the number of neutron populating each time-of-flight channel, over the related energy interval. Without this refinement, we would observe discrete values in the high-energy domain of the spectra or we would need to increase the energy bin size to wash out this effect. During the experiment, lcp detectors or the lead target were moved many times. We verify that the ddcs were identical whatever the configuration inside the vacuum chamber
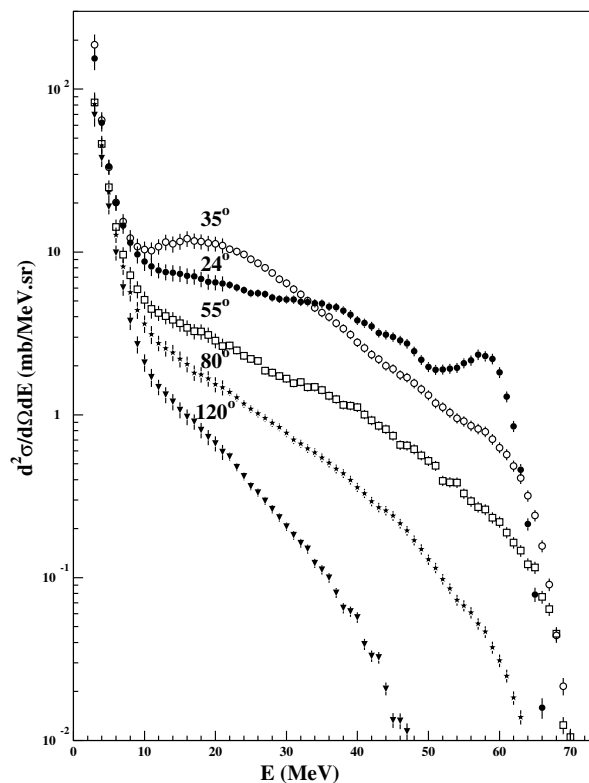
Fig. 14. ^{208}Pb(p, xn) double differential production cross-sections at 62.9 MeV.

Fig. 15. Neutron energy uncertainties as a function of the neutron energy.

was. Doing so, we checked that the different devices do not introduce either neutron scattering or absorption.

In order to evaluate cross-section uncertainties, we combined two different contributions: the detector efficiency uncertainty with the statistical uncertainty over the number of produced neutrons. Over the entire energy range, ddcs relative uncertainties are included in a domain ranging from 5.4% to 15.3%. Only those uncertainties are presented in fig. 14. We seek also for systematical errors. By comparing results obtained in the same experimental conditions, but measured during different periods spread over the entire experimental radiation time, we could observe discrepancies up to 20% for the ddcs extracted at 35° and lower than 10%–15% for the others. Those systematical errors might originate from two effects. The first one might be a slight shift of the beam kicker tuning during the experiment. The swing of the kicker magnet could have been a few pico secondes delayed and a beam tail could have entered inside the experimental area. Systematic errors might also result from blank target runs of different durations which would provide a different precision for the evaluation of the background noise. The energy resolutions were estimated from the time-of-flight path length and the neutron time-of-flight uncertainties. The latter are related to the electronics chain resolution and to the widths of the time-of-flight gamma peaks which are taken as references for the tof determinations. Those estimations lead to uncertainties which increase smoothly

with the neutron energy and which are presented for each detector in fig. 15.

In fig. 14, we observe that the energy spectra are characterised by three components. At high energy, for small angles, we observe a peak which is localised close to the projectile energy and which is associated to direct reactions. A neutron is emitted while the proton undergoes a first or a second collision near the target surface and is absorbed within the nucleus. At low energies, we observe a contribution which is almost constant for all angles and which follows a Maxwellian-like shape. The produced neutrons originate from the evaporation of the heated target which de-excites by emitting particles isotropically. This stage is reached when there has been many collisions which lead to a uniform temperature inside the nucleus. For the intermediate-energy region, the ddcs decrease smoothly. This so-called "pre-equilibrium" component can be explained by processes involved before equilibrium is reached (pre-equilibrium processes). The formed nucleus is not yet thermalized and emits particles while its excitation energy decreases. The pre-equilibrium emission remains at angles as large as 120°, as can be seen in fig. 14.
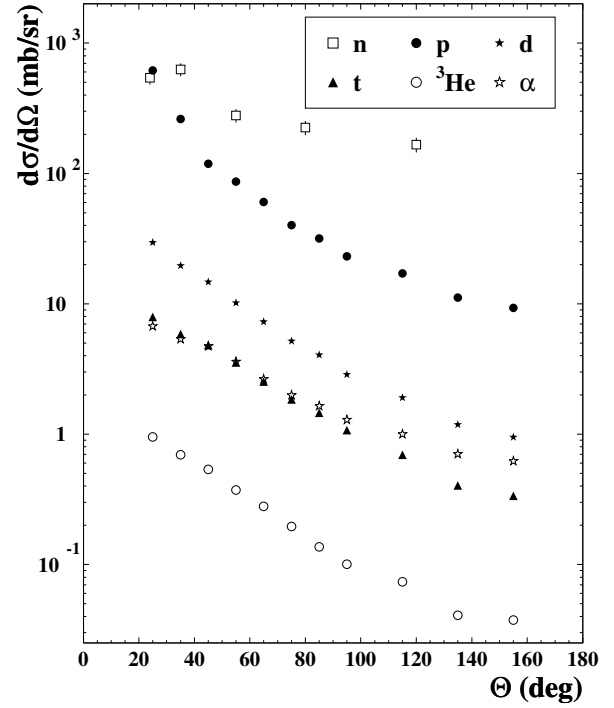
For energies around 20 MeV, we observe that the cross-section increases by a factor of about 1.7 when the detection angle goes from 24° to 35°. In order to explain this raise, we investigated different error sources. We reject the possibility of a spurious behaviour of the neutron counter. Indeed, we performed again this experiment with a new
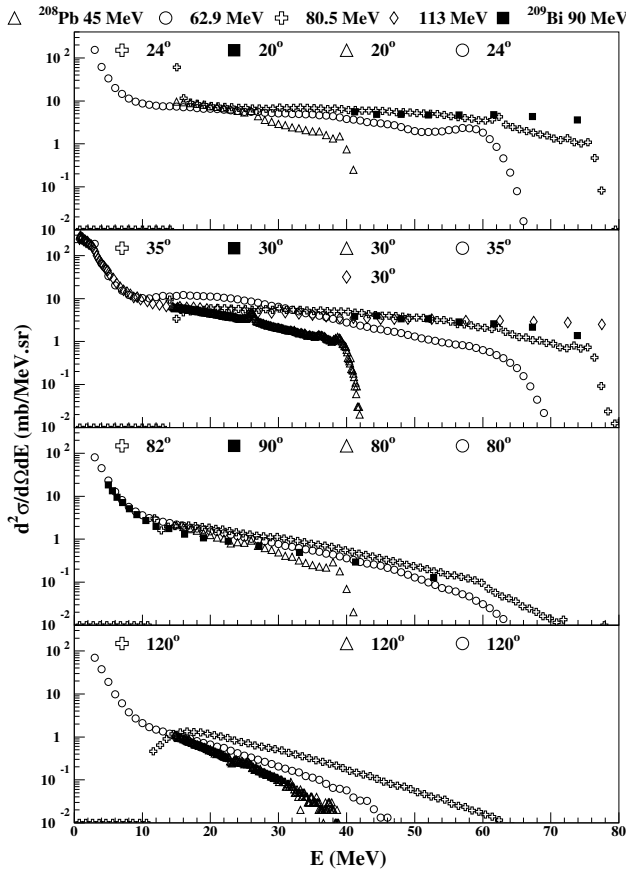
Fig. 16. Neutron ddcs measured in 62.9 MeV ^{208}Pb(p, xn) reactions (circles) compared to experimental data previously measured at 45 MeV (triangles), 80.5 MeV (crosses), 113 MeV (diamonds) on lead, and 90 MeV (squares) on bismuth.

Fig. 17. Angular differential cross-sections for ^{208}Pb(p, xn) and ^{208}Pb(p, $x$lcp) reactions at 62.9 MeV.

set of detectors and we obtained identical results. We also checked that positions of light charged particle detectors have no influence by comparing the production spectra obtained for the set of configurations. Using GEANT simulations [25], we demonstrated that this raise can neither be explained by neutrons which would be scattered, before entering the detector, by the air of the experimental room, the paraffin of the barrels or the steel of the vacuum chamber. Indeed, these neutrons would show up at lower energy due to longer flight path. The alignment of the detectors was done with lasers and a possible very small misalignment would have negligible effect. The discrepancies of a few percent between the DeMoN experimental efficiencies and the KSU predictions, between 10 and 30 MeV, are not sufficient to explain the factor of about 1.7 (58%). Moreover, the energy efficiency dependence has been taken into account in the same way for all detectors and thus, for all angles. Therefore, a bias effect originating from it would have the same consequences for all angles, which is not the case. Finally, in 2001, we redid the measurements with the same experimental set-ups, but for U and Co targets. Preliminary results show that the ratio between cross-sections measured at 24° and 35°, in the 20 MeV region, equals
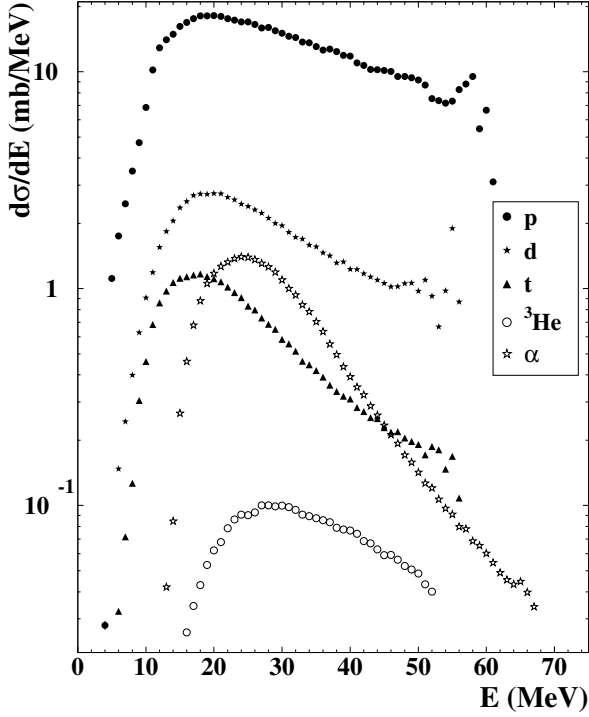
about 2 for U and about 1.1 for Co. So, we can conclude that the effect observed is not related to a detection bias, nor the analysis method employed. In addition, those preliminary results indicate a dependance of the effect with the target atomic number.

In fig. 16, the double differential cross-sections that we measured for the 62.9 MeV ^{208}Pb(p, xn) reactions are compared to experimental data previously estimated by other groups at 45 MeV, 80.5 MeV, 113 MeV on lead [26–29], and 90 MeV on bismuth [30]. In the pre-equilibrium and direct reaction regions, the neutron ddcs measured for 62.9 MeV projectiles (circles) are localised in between those measured for 45 MeV (triangles) and 80.5 MeV (crosses) incident protons, except at 35°, for energies around 20 MeV, were our ddcs are larger than the others. Above 60 MeV, the number of neutrons emitted during direct processes increase with the projectile energy. At low energy, the evaporative component measured at 62.9 MeV is of the same order than those measured at 90 MeV (squares) and 113 MeV (diamonds). From this comparison, we conclude that our data are compatible with neutron ddcs previously measured by other groups.

3.3 Particle angular differential and energy differential cross-sections

It has been possible to extract the angular differential and the energy differential cross-sections from our measurements. The angular differential cross-sections $d\sigma/d\Omega$ were determined by integrating over the energy the double
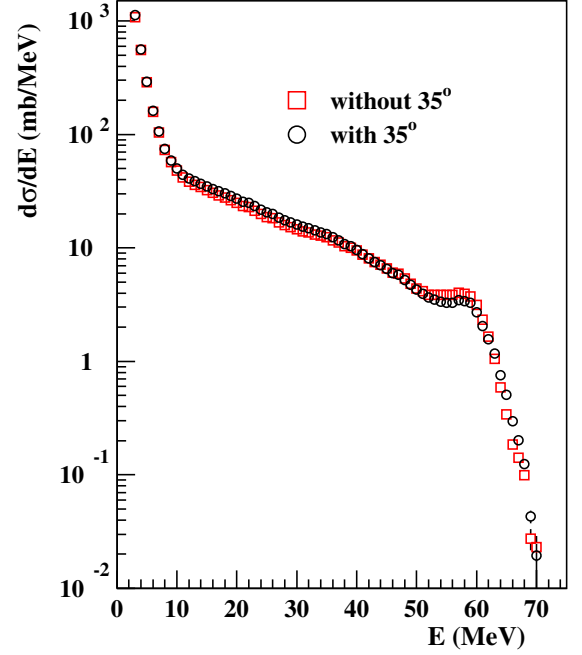
Fig. 18. Light-charged-particle energy differential cross-sections.

Fig. 19. Neutron energy differential cross-sections. Estimations with (opened circles) and without (squares) the ddcs measured at $35°$ are displayed.

differential cross-sections. The distributions obtained for light charged particles and neutrons are presented in fig. 17. In all cases, they all show a non isotropic behaviour because preequilibrium emission is dominant at small angles.

The energy differential cross-sections $d\sigma/dE$ were derived directly by fitting our data points using the Kalbach systematics [31,32]. This systematics successfully accounts for a wide variety of experimental angular distributions of proton-induced reactions at incident energies up to 200 MeV. However it does not take into account correctly direct processes and it is not efficient in energy regions where these processes are dominant. The systematics assumes that emitted particles come from either multistep compound or multistep direct emissions. Kalbach proposes the following formula to fit the curve representing the ddcs defined at a fixed energy, as a function of the emission angle:

$$\frac{d^2\sigma}{d\Omega dE} = \frac{1}{4\pi}\frac{d\sigma}{dE}\frac{P_1}{\sinh(P_1)}(\cosh(P_1\cos\theta) + P_2\sinh(P_1\cos\theta)), \qquad (1)$$

where θ, is the emission angle in the center-of-mass frame, $d\sigma/dE$, P_1 and P_2 are the parameters of the fit. P_1 is a slope parameter and P_2 is the multistep direct emission contribution for the cross-section. By repeating this procedure for each energy, it is possible to construct the energy differential cross-section. The results of the fits are shown in fig. 18 for light charged particles and in fig. 19 for neutrons. The vertical error bars are those given by the

fits. For neutrons, due to the questionable ddcs measured at $35°$, the energy differential cross-section was estimated with (open circles) and without (squares) that angle. We observe that both estimations lead to a slight difference between the extracted differential cross-sections.

In figs. 18 and 19, we recognise the main features that we already pointed out: at low energy, the neutron spectra have a Maxellian-like shape which is associated to the dominant process of evaporation and which cannot be observed with lcp. The following smooth decrease of the distributions are explained by the presence of pre-equilibrium processes. For hydrogen isotope cross-sections, we see that the particle production drecreases with the atomic mass. For helium isotope cross-sections, since ^{4}He is doubly magic the behaviour is different. The triton production is almost one order higher than the ^{3}He production. This difference might be related to the N/Z ratio of the target [24]. We observe a large production of ^{4}He. That might be related to the fact that ^{4}He is easy to produce because it needs only a small amount of energy to be formed.

3.4 Particle production cross-sections

Finally, the production cross-sections were determined by integrating the energy differential cross-sections. They are reported in table 1 for light charged particles and neutrons. The first column indicates the particle type whereas the second column presents the energy range of integration. Indeed, due to the lack of information concerning

Table 1. Production cross-sections obtained in proton-induced reaction on ^{208}Pb at 62.9 MeV.

Particle type	Energy range (MeV)	Data (mb)
p	$2 \leq E \leq 61$	653.0
d	$3 \leq E \leq 55$	80.5
	$3 \leq E$	85.4
t	$4 \leq E \leq 56$	27.0
	$4 \leq E$	27.4
^{3}He	$9 \leq E \leq 52$	2.7
	$9 \leq E$	3.0
α	$10 \leq E \leq 67$	27.9
	$10 \leq E$	28.1
n	$3 \leq E \leq 70$ (with 35°)	3218 ± 203
	(without 35°)	3102 ± 211

direct processes (the Kalbach systematics is not fully appropriate and our most forward angle is equal to 25°), we decided to present the experimental integrated cross-sections both, with a high-energy cut corresponding to the lower limit of the direct process region, and over the full energy range, for all particles but protons and neutrons. The low-energy integration limit is associated to the energy threshold of the detector. For protons, the elastic contribution has been excluded. Table 1 shows that, in spallation reactions, the neutron emission is the dominant channel for the particle production. In addition, we have to notice that 17% of charged particles are composite particles. This is a sizeable percentage which should be taken into account when calculating, for example, energy deposition for target material and geometry optimization, in accelerator-driven-system studies.

4 Comparison with theoretical calculations

Since most of the models only determines $d\sigma/dE$, we decided to make our comparisons directly on that observable. Nevertheless, one must keep in mind that the double differential cross-section observable presents a very sensitive and difficult challenge for the theoretical models since a strong angular dependance exist for many of the processes involved in the particle emissions (see previous sect. 3).

We chose to compare the experimental cross-sections with, on the one hand, the predictions of two event generators widely used inside the nuclear physicist community, which are FLUKA [33] and MCNPX [34], and on the other hand, with the predictions of a new nuclear model code TALYS [35] being developed for the 20 MeV–200 MeV energy range within the HINDAS collaboration. The TALYS code results from a collaboration between NRG-Petten and CEA-Bruyères-le-Châtel. This code intends to describe not only total and partial cross-sections but also energy spectra, angular distributions and double differential cross-sections of neutrons, photons, light charged particles and residues emitted in nuclear reactions. In addition, special attention has been paid to the description of the pre-

**Table 2.** Theoretical production cross-sections.

	MCNPX (INCL4) (mb)	MCNPX (GNASH) (mb)	TALYS (mb)	FLUKA (mb)
Beam energy (MeV)	63	63	62	63
Target	^{208}Pb	^{208}Pb	^{209}Bi	^{208}Pb
Particle type				
p	574.0 (−12%)	963.0 (+47%)	914.4 (+40%)	796.8 (+22%)
full range	574.0	1308.0	914.5	797.4
d		85.2 (+6%)	68.4 (−15%)	
full range		87.3	72.6	
t		9.9 (−63%)	22.7 (−16%)	
full range		10.0	22.7	
^{3}He			2.4 (−11%)	
full range			2.5	
α		11.0 (−60%)	34.5 (+24%)	
full range		11.8	34.6	
n	3191.0 (−1%)	2159.7 (−33%)	2040.5 (−37%)	2144.7 (−33%)
full range	9894.0	7250.02	7232.1	8353.6

equilibrium processes where the two-component exciton model has been extended to an arbitrary number of reaction steps. Our purpose is not to choose between models but rather to show how a new coherent set of data can help theoreticians to improve their predictions. For MCNPX simulations, two different options were alternately tested. At first, the option using the cross-sections evaluated with the GNASH [36] code was chosen. Then, we used the option which calculates the cross-sections with the INCL4 code [37]. For protons, only MCNPX calculates the contribution of the elastic diffusion process. We did not take into account that last process for our comparisons.

The theoretical production cross-sections (cs) are presented in table 2, for various incident proton energies and targets. For each particle type, the theoretical values were obtained by integrating the energy differential cross-sections, either over the same energy range as for the data, or over the full energy range. This last procedure allows to quantify the influence of the experimental energy thresholds. In parentheses are given, in %, the relative differences between theoretical values and data, calculated as follows:

$$\frac{cs_{\text{theory}} - cs_{\text{data}}}{cs_{\text{data}}}. \tag{2}$$

FLUKA is not able to produce composite particle. Therefore, only comparisons with MCNPX(GNASH) and TALYS are given. For all particles, except p cross-sections predicted with MCNPX (GNASH), and neutrons, the experimental energy thresholds have a weak effect on the extracted values. For neutrons, only MCPNX(INCL4)
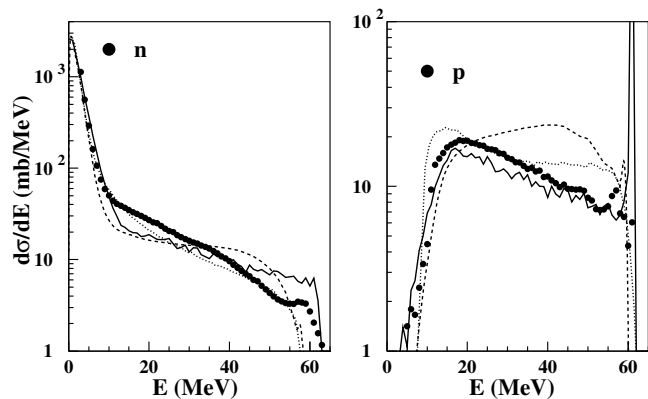
Fig. 20. Neutron and proton energy differential cross-sections. Data are presented as full circles. Theoretical results for MC-NPX(INCL4), TALYS and FLUKA are displayed using, respectively, full, dashed and dotted lines.

predicts a value in very good agreement with the experimental one. All the other codes lead to comparable values which are underestimated by about 35%. For protons, models predict very different values and, again, MCPNX(INCL4) result is the closest to the data, 12% off. We have to point out that the intranuclear cascade code was first develop in order to reproduce data around the GeV range. That unexpected agreement is very promising [38], and it would be interesting to calculate within that model the light-charged-particle production cross-sections. For composite particles, calculated values from different models present large differences. In addition, in some models this contribution is not taken into account although our experiment shows that these particles correspond to 17% of the total charged-particle reaction cross-section. We also notice a big improvement between MCNPX (GNASH) and TALYS capabilities. For TALYS, the largest differences with the experimental production cross-sections, is for alpha particles which are 24% overestimated.

The comparison between experimental energy differential cross-sections and theoretical calculations are presented for the (p, xn) and (p, xp) channels in fig. 20. The data are shown as full circle whereas MCNPX(INCL4), TALYS and FLUKA predictions are displayed, respectively, using full, dashed and dotted lines. For MCNPX simulations, only spectra predicted with the INCL4 option are presented because that last gives the best agreement with the experimental production rates. For neutrons, the evaporative component is well reproduced by all codes. For the pre-equilibrium region and at high energy, we do observe discrepancies between the experimental and calculated data. Depending of the energy region considered, they underestimate or overestimate the data. Even worth, the different models are not in agreement even though they give similar production values (GNASH, TALYS, FLUKA) or predict correctly the experimental rate (INCL4). For the proton production differential cross-section, only MCNPX(INCL4) reproduces correctly the experimental shape. The other codes overestimate the pro-
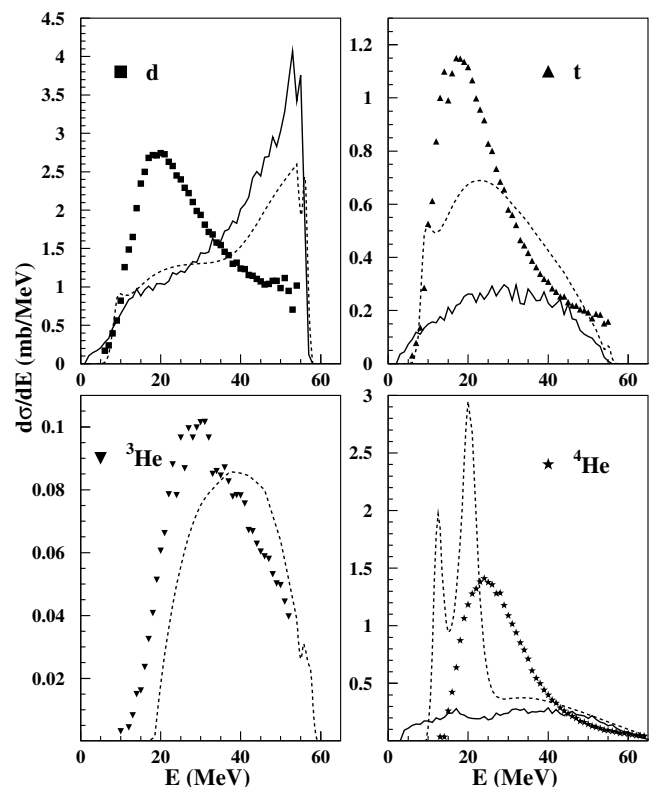
Fig. 21. Energy differential cross-sections for d, t, ^{3}He and alpha-particle are presented as full circles for experimental data, theoretical results for MCNPX(GNASH) and TALYS are displayed using respectively full and dashed lines.

duction at high energy. This effect is probably related to the underestimation which we noted for the neutron production rates with all codes except MCNPX(INCL4).

Since FLUKA and INCL4 do not produce any composite particle, for the (p, xd), (p, xt), (p, x^3He) and $(p, x\alpha)$ energy differential cross-sections, only comparisons with MCNPX(GNASH) and TALYS results are shown in fig. 21. The performance in reproducing the composite-particle spectra depends drastically on the particle. For deuteron (upper left panel in 21) neither TALYS nor MC-NPX give the correct shape, even if the integrated cross-section are quite good (see table 2). For triton and alpha-particles (right panels in 21), TALYS produces more composite particles than MCNPX but neither the shape nor the amplitude of the spectra correspond to the data. Only for ^{3}He an agreement can be found between the data and the TALYS calculation. This comparison shows that the theoretical models still need to be improved, and in particular the composite particle production channel.

5 Conclusion

Neutron and light-charged-particle double differential cross-sections have been measured in 62.9 MeV proton-induced reactions on ^{208}Pb target. For hydrogen and

helium isotopes, values have been extracted over eleven angular positions from 25° to 155°. For neutrons, the ddcs were measured at five different angles (24°, 35°, 55°, 80° and 120°). The angular differential and energy differential cross-sections, as well as the production cross-sections have also been derived.

A comparison has been made with calculated data from FLUKA and MCNPX (two event generators widely used inside the community) and a nuclear model code TALYS, developed within the HINDAS collaboration. Some discrepancies have been observed at high energy for both neutrons and protons. The neutron and proton productions are well predicted by MCNPX, using the option with INCL4. The other codes underestimate the neutron rate whereas they overestimate the proton one. For composite particles which represent 17% of the charged particle production cross-section, neither the shape nor the amplitude of the cross-sections are correctly predicted by any model. The experimental results presented in this paper have been sent to the Nuclear Energy Agency in order to be added to the nuclear reaction data bank. They are part of a coherent set of data measured on lead around 63 MeV. Other targets (Fe/Co and U) and incident energy (135 MeV) are still under analyses. Reactions with incident neutrons at 63 MeV and 96 MeV have also been performed in order to enrich this set. All these data will be soon available and will allow a better understanding of the mechanisms responsible for the particle production in the energy range between 20 MeV and 200 MeV.

References

1. N. Morishima, Nucl. Data News **62**, 2 (1999).
2. B.P. Schoenborn *et al.*, J. Neutron Res. **7**, 89 (1999).
3. M. Angelone, S. Atzeni, S. Rollet, Nucl. Instrum. Methods Phys. Res. A **487**, 585 (2002).
4. J.F. Ziegler, IBM J. Res. Dev. **40**, 91 (1996).
5. C.D. Bowman *et al.*, Nucl. Instrum. Methods Phys. Res. A **320**, 336 (1992).
6. C. Rubbia *et al.*, CERN/AT95-44(ET) (1995).
7. I.S.K. Gardner *et al.*, Nucl. Instrum. Methods Phys. Res. B **139**, 82 (1998).
8. G.S. Bauer, M. Salvatores, G. Heusener, J. Nucl. Mater. **296**, 17 (2001).
9. The European Technical Working Group on ADS, *A European Roadmap for Developing Accelerator Driven Systems (ADS) for Nuclear Waste Incineration* (ENEA Communication and Information Unit, Rome, 2001).
10. Cross-Section Evaluation Working Group, ENDF/B-VI Summary Documentation, Report BNL-NCS-17541 (ENDF-201) (1991), edited by P.F. Rose, National Nuclear Data Center, Brookhaven National Laboratory, Upton, NY, USA.
11. *The JEF-2-2 Nuclear Data Library*, JEFF Report 17, OECD Nuclear Energy Agency (2000).
12. A. Boudard, J. Cugnon, S. Leray, C. Volant, Phys. Rev. C **66**, 044615 (2002).
13. A.J. Koning, J.P. Delaroche, O. Bersillon, Nucl. Instrum. Methods Phys. Res. A **414**, 49 (1998).
14. European community contract number FIKW-CT-2000-00031 *HINDAS: High and Intermediate Energy Nuclear Data for Accelerator-driven Systems* (2000); A.J. Koning *et al.*, *Proceedings of the International Conference on Nuclear Data for Science and Technology, October 7-12, 2001, Tsukuba, Ibaraki, Japan*, edited by K. Shibata, J. Sci. Technol., Suppl. **2**, 1161 (2002).
15. M. Kerveno *et al.*, Phys. Rev. C **66**, 014601 (2002).
16. J. Klug *et al.*, Nucl. Instrum. Methods Phys. Res. A **489**, 282 (2002).
17. I. Tilquin *et al.*, Nucl. Instrum. Methods Phys. Res. A **365**, 446 (1995).
18. E. Bauge *et al.*, Phys. Rev. C **61**, 034306 (2000).
19. C. Varignon, PhD Thesis, LPC Caen (1999).
20. R.A. Cecil *et al.*, Nucl. Instrum. Methods Phys. Res. **161**, 439 (1979).
21. F. Borne, PhD Thesis, Bordeaux I (1998).
22. F.R. Lecolley, PhD Thesis, LPC Caen (1996).
23. J.R. Wu, C.C. Chang, H.D. Holmgren, Phys. Rev. C **19**, 659 (1979).
24. F.E. Bertrand, R.W. Peelle, Phys. Rev. C **8**, 3 (1973).
25. CERN program library long write-up W5013 *GEANT: Detector Description and Simulation Tool* (1993).
26. Galonsky *et al.*, Phys. Rev. C **12**, 378 (1975).
27. M. Blann, R.R. Doering, Aaron Galonsky, D.M. Patterson, F.E. Serr, Nucl. Phys. A **257**, 15 (1976).
28. M. Trabandt, W. Scobel, M. Blann, B.A. Pohl, R.C. Byrd, C.C. Foster, R. Bonetti, Phys. Rev. C **39**, 452 (1989).
29. M.M. Meier, D.A. Clark, C.A. Goulding, J.B. McClelland, G.L. Morgan, C.E. Moss, W.B. Amian, Nucl. Sci. Eng. **102**, 310 (1989).
30. A.M. Kalend, B.D. Anderson, A.R. Baldwin, R. Madey, J.W. Watson, C.C. Chang, H.D. Holmgren, R.W. Koontz, J.R. Wu, H. Machner, Phys. Rev. C **28**, 105 (1983).
31. C. Kalbach, F.M. Mann, Phys. Rev. C **23**, 112 (1981).
32. C. Kalbach, Phys. Rev. C **37**, 2350 (1988).
33. A. Ferrari, P.R Sala, *Proceedings of the MC93 International Conference on Monte Carlo Simulation in High Energy and Nuclear Physics, Tallahassee, Florida* (World Scientific, Singapore, 1993) p. 277.
34. LA-UR-03-5916 MCNPX, version 2.5.D (2003).
35. A.J. Koning *et al.*, *Proceedings of the International Conference on Nuclear Data for Science and Technology, October 7-12, 2001, Tsukuba, Ibaraki, Japan*, edited by K. Shibata, J. Sci. Technol., Suppl. **2**, 1491 (2002).
36. P.G. Young, E.D. Arthur, M.B. Chadwick, *Comprehensive nuclear model calculations: introduction to the theory and use of GNASH code*, internal report LA-12343-MS (1992).
37. A. Boudard *et al.*, Phys. Rev. C **66**, (2002) 044615.
38. J. Cugnon, P. Henrotte, Eur. Phys. J. A **16**, 393 (2003).